Monthly Notices of the ROYAL ASTRONOMICAL SOCIETY

MNRAS **547,** 1–11 (2026) https://doi.org/10.1093/mnras/stag385
Advance Access publication 2026 February 26

Tiny galaxies and dark substructures: exploring the 'dark' subhaloes in TNG50

Jessica E. Doppel [1,2★] Mathilde Jauzac,[1,2,3,4] David J. Lagattuta [1,2,5] Azadeh Fattahi [2,6] and Guillaume Mahler[1,2,7]

[1]*Centre for Extragalactic Astronomy, Durham University, South Road, Durham DH1 3LE, UK*
[2]*Institute for Computational Cosmology, Durham University, South Road, Durham DH1 3LE, UK*
[3]*Astrophysics Research Centre, University of KwaZulu-Natal, Westville Campus, Durban 4041, South Africa*
[4]*School of Mathematics, Statistics & Computer Science, University of KwaZulu-Natal, Westville Campus, Durban 4041, South Africa*
[5]*Centre for Astrophysics Research, Department of Physics, Astronomy and Mathematics, University of Hertfordshire, Hatfield AL10 9AB, UK*
[6]*The Oskar Klein Centre, Department of Physics, Stockholm University, Albanova University Center, SE-10691 Stockholm, Sweden*
[7]*STAR Institute, Quartier Agora – Allée du six Août 19c, B-4000 Liège, Belgium*

Accepted 2026 February 21. Received 2026 January 27; in original form 2025 May 23

ABSTRACT

Dark matter haloes and subhaloes that host no luminous counterpart are predicted within our current understanding of galaxy formation within a ΛCDM (Λ cold dark matter) paradigm. Observational tests, such as gravitational lensing, have made potential detections of such objects around individual galaxies as well as in galaxy groups and clusters. The question of whether or not a dim counterpart might reside in these objects remains an open question. We investigate this point using the TNG50-1 simulation of the IllustrisTNG project. Under the assumption of TNG50's galaxy formation model, we do not find haloes or subhaloes above a total mass of $10^{9.7}\,M_\odot$ that are entirely dark. However, under realistic effective surface brightness cuts of $\leq$29 mag arcsec^{-2}, the inference of the most massive dark subhalo in galaxy groups and clusters becomes $M_{\rm DM} \gtrsim 2 \times 10^{10}\,M_\odot$. Concentrating on galaxy groups and clusters, we find that dark subhaloes are ubiquitous, with more massive dark subhaloes tending to preferentially reside further from the centres of clusters. Subhaloes in the mass range of $4.5 \times 10^7 \leq M_{\rm DM}/M_\odot \leq 2.1 \times 10^8$ tend to be the most likely to reside in the strong lensing regions of galaxy groups and clusters, and argue that future dark subhalo searches should investigate this mass range.

Key words: galaxies: clusters: general – galaxies: dwarf – galaxies: haloes.

1 INTRODUCTION

Λ cold dark matter (ΛCDM; e.g. S. D. M. White & M. J. Rees 1978; S. D. M. White & C. S. Frenk 1991) has proven one of the most successful cosmological frameworks to date (e.g. L. V. Sales, A. Wetzel & A. Fattahi 2022; M. Gámez-Marín et al. 2024; I. S. Sands et al. 2024). It predicts the hierarchical formation of structure from tiny, low-mass haloes that merge into the galaxies, galaxy groups, and galaxy clusters that we see today. Adding model of galaxy formation onto the predictions of ΛCDM suggests that there should be dark matter haloes in which galaxies are unable to form (e.g. M. J. Rees 1986; G. Efstathiou 1992; T. Quinn, N. Katz & G. Efstathiou 1996; A. A. Thoul & D. H. Weinberg 1996; R. Barkana & A. Loeb 1999), leading to a population of aptly named dark subhaloes in semi-analytical and semi-empirical models (e.g. J. S. Bullock, A. V. Kravtsov & D. H. Weinberg 2000; A. J. Benson et al. 2002; E. O. Nadler et al. 2020, 2024; E. O. Nadler 2025) and cosmological hydrodynamical simulations (e.g. T. Sawala et al. 2016; E. D. Jahn et al. 2019; V. J. Forouhar Moreno et al. 2022; G. Lee et al. 2024). Under different model assumptions (and resolutions) in these scenarios, the mass at which haloes cease to form galaxies varies (e.g. T. Sawala et al. 2013, 2016; A. Benitez-Llambay & C. Frenk 2020; F. Munshi et al. 2021; S. Y. Kim et al. 2024). Thus, it is an open question at what scale one should expect to see haloes that are entirely dark.

Testing the predictions for the existence of dark-matter-only objects observationally is, however, exceedingly difficult. Currently, direct detections of dark matter have remained elusive (see L. E. Strigari 2013, for a review). Thus, only indirect methods are available to infer the existence of such substructures. At different scales and distances, different observational techniques must be invoked. Around the Milky Way, particularly in the solar neighbourhood, instruments such as *Gaia* (Gaia Collaboration 2016) allow for the observation of the full 6D phase space of individual stars. This facilitates the use of dynamical methods to potentially connect the gaps with past interactions with dark substructures or, perhaps, with luminous objects of similar mass (see e.g. W. Dehnen et al. 2004; J. H. Yoon, K. V. Johnston & D. W. Hogg 2011; R. G. Carlberg 2012; A. Bonaca et al. 2019).

For extragalactic targets, where full phase-space information cannot be obtained, a different sort of methodology is necessary to search for dark objects. One such method involves the use of strong gravitational lensing (e.g. P. Natarajan et al. 2024). The way

★ E-mail: jessicadoppel@gmail.com

in which images of background galaxies are multiplied, deflected, distorted, and magnified by a foreground galaxy or galaxy cluster can be used to infer the mass distribution of that galaxy (cluster) (e.g. M. Jauzac et al. 2014; J. M. Diego et al. 2018; G. Mahler et al. 2023; C. Cerny et al. 2025). Additional distortions to images or anomalies in magnification can be used to detect the presence of nearby substructure. Potential (dark) subhalo detections have been made using galaxy-scale lenses (e.g. S. Vegetti et al. 2010, 2012; A. M. Nierenberg et al. 2014; Y. D. Hezaveh et al. 2016; S. C. Lange et al. 2025) and within galaxy clusters (e.g. J. M. Diego et al. 2022, 2023). These detected objects have masses between $\sim 10^8$ and 10^9 $M_\odot$ (with the exception of J. M. Diego et al. 2023, which finds a subhalo mass of 2.5×10^6 $M_\odot$), which puts them in the regime where it may be possible to host faint dwarf galaxies that would require very deep and high-resolution imaging to detect.

Given both the richness of galaxy clusters, as well as the influx of new results from strong lensing cluster surveys from, e.g. *James Webb Space Telescope* (e.g. C. Cerny et al. 2025) and *Euclid* (Euclid Collaboration 2025), these systems are positioned as excellent targets for subhalo searches. The majority of lensing clusters tend to reside between $z \sim 0.1$ and 0.6 (see e.g. M. Postman et al. 2012; L. E. Bleem et al. 2015; D. Coe et al. 2019; K. Sharon et al. 2020; J. Richard et al. 2021; C. Fox et al. 2022), with a handful of such clusters residing above $z \gtrsim 1$ (E. J. Gonzalez et al. 2015). It is observationally challenging in this redshift range to detect low-mass galaxies, as both very deep imaging and very high spatial resolution are necessary to detect subhaloes using strong lensing. This adds a complicating factor to the detection of truly dark subhaloes: are they truly dark, or do they contain tiny galaxies? In the last decade (or so), there has been an influx of observations of Local Group dwarf and ultrafaint satellites (see J. D. Simon 2019, and references therein). There is substantial overlap between the predicted dark matter masses of these tiny galaxies from abundance matching studies (e.g. R. H. Wechsler & J. L. Tinker 2018; M. Shuntov et al. 2022, 2025; J. S. Monzon, F. C. van den Bosch & K. Mitra 2024) and simulations (e.g. N. Ahvazi et al. 2024; S. Y. Kim et al. 2024; M. P. Rey et al. 2025), and the masses of subhaloes possibly detected from lensing studies ($M_{\rm sub} \sim 10^9$ $M_\odot$; e.g. S. Vegetti et al. 2014).

In order to understand the dwarf and dark (sub)halo populations in galaxy clusters and in the field, we need to turn to cosmological hydrodynamical simulations of large cosmological volumes. Ideally, investigating large enough volumes to contain massive systems like lensing clusters at $z \lesssim 1$ would provide the most direct comparison. However, simulations that fit this criterion often have particle masses $>10^6$ $M_\odot$ (e.g. S. Genel et al. 2014; M. Vogelsberger et al. 2014; R. A. Crain et al. 2015; J. Schaye et al. 2015, 2023; A. Pillepich et al. 2018); thus, low-mass dwarfs and dark subhaloes cannot be reliably resolved in these simulations. We therefore opt to use the IllustrisTNG50 simulation (D. Nelson et al. 2019a, b; A. Pillepich et al. 2019), as it has a high enough resolution ($m_{\rm DM} = 4.5 \times 10^5$ $M_\odot$, $m_{\rm baryon} = 8.4 \times 10^4$ $M_\odot$) to study the low-mass objects in question in realistic galaxy group and cluster environments.

This paper is organized as follows. In Section 2, we briefly discuss the simulation and the selection criteria. In Section 3, we discuss the expected mass function of dark subhaloes, the halo occupation fraction, and the distribution of dark substructures in galaxy clusters. We present a brief discussion of the interpretation of our results in strong-lensing-based subhalo searches in Section 4. Finally, we conclude with a summary of our results in Section 5.

2 METHODS

2.1 Simulations

We use the highest resolution run of the cosmological hydrodynamical simulation TNG50 (D. Nelson et al. 2019b; A. Pillepich et al. 2019) due to its ability to simultaneously resolve low-mass objects and galaxy cluster environments. TNG50 is the smallest volume of the larger IllustrisTNG project (F. Marinacci et al. 2018; J. P. Naiman et al. 2018; D. Nelson et al. 2018, 2019a; A. Pillepich et al. 2018; V. Springel et al. 2018), featuring a box size of 51.7 Mpc on one side and 2×2160^3 gas cells and dark matter particles. The simulation is evolved from a flat, ΛCDM cosmology using cosmological parameters from Planck Collaboration XIII (2016). The simulation has a mass resolution of 4.5×10^5 $M_\odot$ for individual dark matter particles, an average mass of 8.4×10^4 $M_\odot$ for star and gas particles, and a gravitational softening length of 288 pc at $z = 0$.

Gravity and hydrodynamics in TNG50 are solved using AREPO. Heating and cooling of gas is followed down to 10^4 K in an effective equation of state interstellar medium (ISM). TNG50's galaxy formation model includes star formation in the dense ISM stellar evolution (including supernova and chemical enrichment of the ISM). Heating of the gas occurs via background radiation, and cooling includes metal line cooling and primordial cooling. Additionally, the model includes the seeding and growth of supermassive black holes, active galactic nuclei feedback from both low- and high-accretion modes, and magnetic fields (R. Pakmor, A. Bauer & V. Springel 2011; R. Pakmor & V. Springel 2013; R. Weinberger et al. 2017; A. Pillepich et al. 2018).

2.2 Galaxy and subhalo selection

Haloes are identified in TNG50 using the friends-of-friends algorithm (FoF; M. Davis et al. 1985) with a linking length of 0.2 times the mean interparticle separation, and subhaloes within those haloes are further identified using SUBFIND (V. Springel et al. 2001; K. Dolag et al. 2009). Halo masses and radii are characterized by the total mass enclosed within a radius containing 200 times the critical density of the Universe.

In order to remain as close as possible to studies of dark substructures in galaxy clusters (e.g. using strong gravitational lensing; see D. J. Lagattuta et al. 2023; G. Mahler et al. 2023), we chose to investigate the progenitors of the three most massive galaxy clusters at $z = 0$. The most massive cluster ($M_{200,c} = 1.83 \times 10^{14}$ $M_\odot$) is roughly consistent with low-end mass estimates of the Virgo Cluster ($M_{200,c} \sim 2 \times 10^{14}$ $M_\odot$; S. M. Weinmann et al. 2011), with the other two ($M_{200,c} = 9.41 \times 10^{14}$ $M_\odot$ and $M_{200,c} = 6.46 \times 10^{13}$ $M_\odot$) on par with massive galaxy groups, such as Fornax ($M_{200,c} \sim 10^{14}$ $M_\odot$; M. J. Drinkwater, M. D. Gregg & M. Colless 2001) at $z = 0$. We follow the main-branch progenitors of these objects through in time using the SUBLINK merger tree (V. Rodriguez-Gomez et al. 2015). We consider the progenitors of these objects beginning at $z = 2$, and follow them at intervals of $dz \sim 0.2$. This allows us to understand how the population of low-mass subhaloes associated with these structures changes over time.

While it should be noted that these systems are less massive than strong lensing clusters, they allow us to probe the population of low-mass subhaloes that cannot be investigated in the simulations that resolve more massive systems. We therefore opt to leave results normalized by virial quantities when possible. Given the self-similarity predicted by ΛCDM, this allows for our results to be extrapolated to more massive systems, noting that only a change in normalization in each of our relations should occur as halo mass changes (e.g. J. Han et al. 2016).

Within the selected clusters, their progenitors, and the field, we choose (sub)haloes that have a total dark matter mass – the sum of all dark matter particles considered associated with an object via SUBFIND – of at least $M_{\rm DM} = 4.54 \times 10^7\,{\rm M}_\odot$, ensuring that they are resolved by at least 100 particles. We invoke an upper dark matter mass limit of $M_{\rm DM} = 2 \times 10^{10}\,{\rm M}_\odot$. The luminous components are considered resolved if they have 100 star particles associated with them, resulting in an average stellar mass of $M_* \gtrsim 8 \times 10^6\,{\rm M}_\odot$.

2.3 Surface brightness calculation

We additionally consider an 'observationally' resolved limit, which is made in addition to the aforementioned star particle number cut. We make this cut based on brightness limits *as they are observed at* $z = 0$, which we take to be 29 mag arcsec^{-2}. This is roughly on par with the brightness limit of the Frontier Fields survey (D. Coe, L. Bradley & A. Zitrin 2015; J. M. Lotz et al. 2017), which is considered state of the art for the *Hubble Space Telescope*, although it is larger than the brightness limits from e.g. the GLIMPSE (Galactic Legacy Infrared Mid-Plane Survey Extraordinaire) deep fields (H. Atek et al. 2025).

We make the assumption that half of the light (as recorded by the SUBFIND catalogues) is contained within the stellar half-mass radius, $R_{\rm h,*,projected} = 0.75 r_{\rm h,*,3D}$, of a galaxy. We have explicitly checked using particle data that this assumption holds for most target galaxies. We then take the average surface brightness within $r_{\rm h,*}$ and make a 'mock observation' of the galaxy at its given redshift. We assume a flat ΛCDM cosmology, with the cosmological parameters used by the simulation, i.e. $\Omega_{\rm ma,0} = 0.3089$, $\Omega_{\Lambda,0} = 0.6911$, and $h = 0.6774$. We additionally utilize the recorded redshift and scale factor of the relevant snapshots to calculate cosmological distances. We calculate the comoving radial distance to each object using

$$r = \frac{c}{H_0} \int_0^z \frac{{\rm d}z'}{\sqrt{\Omega_{\rm M}(1+z')^3 + \Omega_\Lambda}}, \tag{1}$$

using the simulation parameters mentioned above. To calculate the angular size of our object, we first calculate the angular diameter distance, $d_{\rm A}$, at the given redshift following:

$$d_{\rm A} = \frac{r}{(1+z)}. \tag{2}$$

We can then find the angle subtended by the half-mass radius of the galaxy:

$$\theta = R_{\rm h,*,proj}/d_{\rm A}. \tag{3}$$

To find surface brightness in terms of mag arcsec^{-2}, we calculate the cosmological distance modulus using

$$m = M + 5\log_{10}(d_{\rm L}) + 25, \tag{4}$$

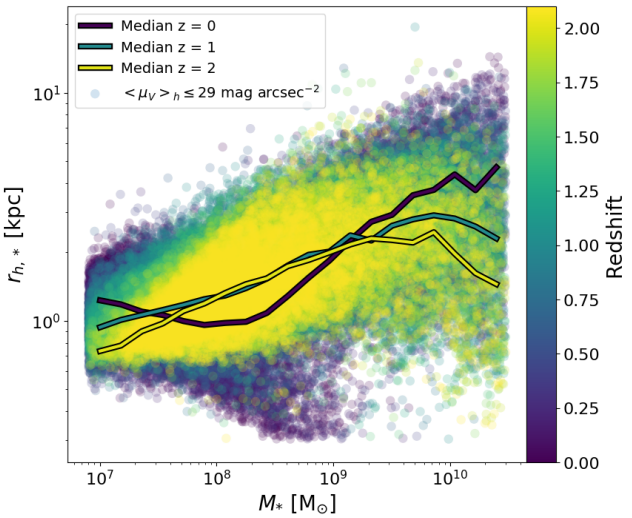

Figure 1. Stellar half-mass radius ($r_{\rm h,*}$) as a function of stellar mass (M_*). Each point represents an object at the redshift indicated by the colour bar. Median lines are shown for redshifts 0, 1, and 2. We note the presence of a few extremely compact objects that reside in the field at $z = 0$ that pull the median line down in the range $10^8 \leq M_*/{\rm M}_\odot \leq 10^9$. Taking that into account, we can see that the surface brightness cut of $\langle\mu_V\rangle_{\rm h} = 29$ mag arcsec^{-2} introduces a bias towards detecting only the more compact systems at fixed stellar mass for particularly low-mass galaxies.

where $d_{\rm L} = d_{\rm A}(1+z)^2$ is the luminosity distance. For galaxies at $z = 0$, we assume they sit at the distance of the Virgo Cluster (16.5 Mpc; e.g. S. Mei et al. 2007).

Imposing a surface brightness cut effectively introduces a bias into our sample, which is illustrated by the (physical) size–mass relation in Fig. 1. We show median relations between stellar half-mass radius ($r_{\rm h,*}$) and stellar mass (M_*) as lines coloured by their respective redshifts for $z = 0, 1, 2,$ At low redshift, the surface brightness cut accounts for all resolved dwarfs within our selected mass range. At fixed particle number (stellar mass), we select for more compact objects or objects. The relationship between stellar mass and stellar half-mass radius agrees reasonably well with observations at $z = 0$ (A. Pillepich et al. 2019). It should be noted that we do not resolve the scales of e.g. nuclear star clusters and ultracompact dwarfs that could help in the identification of lower mass galaxies that otherwise are not picked up by the surface brightness cut.

At $z = 0$, the brightness cut identifies all but 155 targeted, particle-number-selected galaxies, 130 of which have $M_* \leq 1.2 \times 10^7\,{\rm M}_\odot$, and account for 10 per cent of the galaxies in that mass bin. Higher mass bins are not significantly affected by the cut. Given that observed surface brightness decreases with redshift by a factor of $(1+z)^{-4}$ in our assumed cosmology, we should expect the lower mass bins in particular to be more significantly impacted at higher z. At $z = 1$, within the same stellar mass bin as examined previously ($M_* \leq 1.2 \times 10^7\,{\rm M}_\odot$), only 32 per cent of galaxies meet the surface brightness criteria. Interestingly, there are only three 'visible' galaxies within the selected group progenitors in this mass bin. Of all galaxies at $z = 1$ that satisfy the particle cut, 18 per cent do not satisfy the surface brightness cut. By $z = 2$, 8 out of 2760 resolved galaxies in this lowest mass bin pass the surface brightness requirement, with only 47 per cent of the total set of resolved galaxies meeting the requirement across all mass bins.

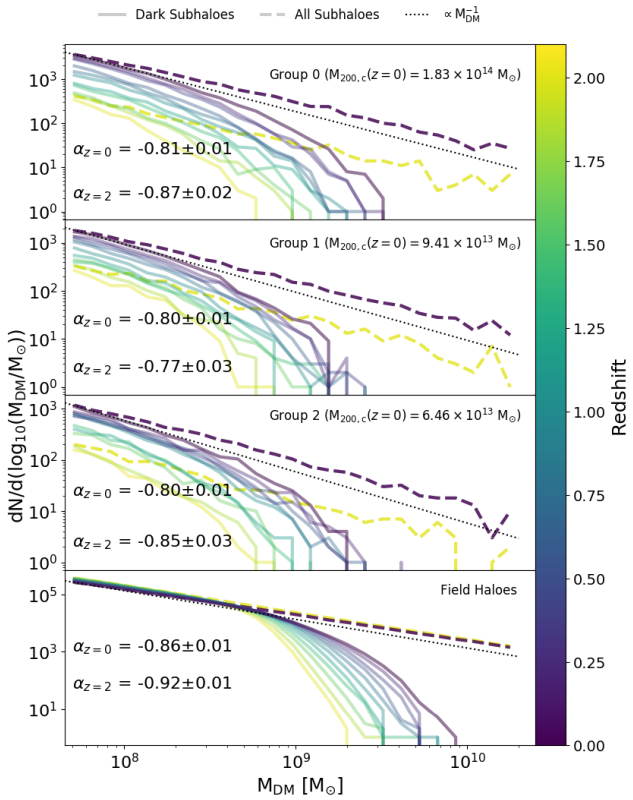

Figure 2. Top three panels: Subhalo mass functions for the three galaxy groups and clusters considered in this study over the redshift range $z = 0$–2. We consider only the subhaloes associated with these systems in the SUBFIND catalogues. Bottom panel: Halo mass functions for field haloes, i.e. those that are considered their own centrals. In all panels, the mass functions of all (sub)haloes are shown in the dashed lines, and for the entirely dark (sub)haloes ($M_* = 0$ and $M_{\rm gas} = 0$) in the solid lines. All lines are coloured by the redshift at which they are measured, with lighter colours indicating higher redshift and darker colours lower redshift. For comparison, we show the expected slope of the halo mass function in the black dotted line (see J. S. Bullock & M. Boylan-Kolchin 2017, and references therein), and we print the best-fitting slopes of the simulation's mass function at $z = 0$ and $z = 2$.

Finally, we do note that the choice of an observational cut was made to be on par with relatively deep surveys, and was not chosen to mimic any one instrument or any specific survey. The 'mock observations' are therefore intended as a toy model meant to impose a more physical limit on our selection. We do not take into account confusion, etc., because the intent is not to be a rigorous mock observation, but to understand the distribution of dark and light objects in realistic galaxy cluster environments. We do, however, discuss the impacts of such surface brightness cuts in Sections 3 and 5.

3 RESULTS

3.1 Dark matter (sub)halo mass function

To begin to characterize the dark objects that reside within the simulation volume, we first consider the mass function of all low-mass subhaloes considered in this study. The top three panels of Fig. 2 show the subhalo dark matter mass functions for the three galaxy groups and clusters considered in this study (Groups 0, 1, and 2) and their main progenitors at higher redshift, with the bottom panel showing the same but for field haloes within the considered redshift range. Of the objects investigated in this study, roughly 3 per cent of them reside in our target clusters at $z = 0$.

In Fig. 2, we can see the expected slopes in the mass functions for subhaloes in both the groups and clusters and haloes in the field (dashed lines colored by redshift). Following previous studies (e.g. S. Ghigna et al. 1998; R. K. Sheth, H. J. Mo & G. Tormen 2001) and as discussed in J. S. Bullock & M. Boylan-Kolchin (2017), we find that subhaloes in clusters follow a shallower slope than field haloes, which are theoretically expected to follow $\mathrm{d}n/\mathrm{d}(\log_{10}(M_{\rm DM}) \propto M_{\rm DM}^{\alpha}$, where $\alpha = -1$. We do not see a significant flattening out of the slope in the low-mass end that would indicate the presence of resolution effects.

Focusing on what is entirely dark ($M_* = 0$, $M_{\rm gas} = 0$), we can see some slight differences between the mass functions of the subhaloes and field haloes. While these are not volume densities of (sub)haloes, we do find lower upper-end mass cut-offs and an earlier deviation from the total mass function in clusters than in the field. As haloes enter cluster environments, what substructure finders designate as the 'edge' of a subhalo becomes less clear than for the same object in the field (see e.g. F. C. den Bosch et al. 2018; V. J. Forouhar Moreno et al. 2025). Across all masses investigated in this work, we find a median of 6 per cent dark matter mass loss between the time of infall and the following snapshot in the simulation. Additionally, in the field, a dark halo can continue to accrete mass, whereas within a cluster environment, high velocities within the cluster potential make it very difficult for subhaloes to continue to grow (e.g. S. Ghigna et al. 1998). The dark subhaloes will, as expected, only lose mass as they continue to interact with the cluster environment (e.g. B. Moore et al. 1996; O. Y. Gnedin 2003; D. Nagai & A. V. Kravtsov 2005; R. Smith et al. 2016; A. Niemiec et al. 2019). For all dark subhaloes in our target clusters at $z = 0$, for example, we find a median infall redshift of $z \sim 0.16$ and a retained dark matter fraction of $M_{\rm DM,z=0}/M_{\rm DM,infall} = 0.72$. The difference between the upper-end cut-off in the mass function between the cluster and the field can therefore be explained with a combination of numerical mass fluctuations, the lack of subhalo growth, and tidal stripping after entering a cluster.

Finally, we do not find the stripping of luminous components, e.g. stars and gas, to be a driving factor for the emergence of the population of dark subhaloes. In fact, within the lowest mass bin explored in Section 3.5 ($7.62 \leq M_{\rm DM} \leq 8.32$), only 6 per cent of dark subhaloes have ever hosted a stellar component, none of which have been considered resolved by this study. This is in line with results from G. Lee et al. (2024), who find that their sample of dark galaxies tends to originate in voids and possesses little to no star-forming gas.

3.2 Galaxy occupation fraction

One aspect that should be noted in the interpretation of entirely dark subhaloes in TNG50 (or a similar sort of simulation) is that the stellar mass of the galaxies that they could contain may be smaller than the mass of the baryonic resolution element within the simulation. It could be argued that these dark objects simply host an *unresolved* stellar component. In order to circumvent this limitation, we instead turn our focus to what is *observationally* dark. As mentioned in Section 2, we consider a galaxy resolved if it has at least 100 star particles, and we place an additional surface

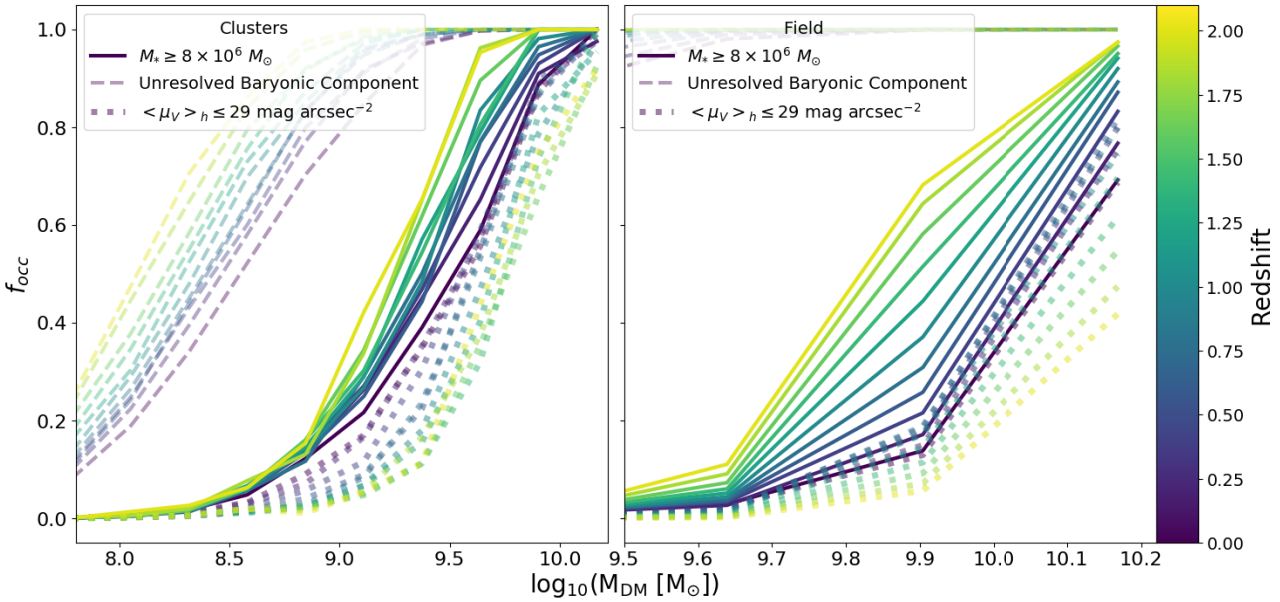

Figure 3. Occupation fraction of dark matter subhaloes at different redshifts. We show the occupation fraction of dark matter haloes for three different sets of galaxies: those that are resolved by particle number (solid lines), those that are above a surface brightness limit of 29 mag arcsec^{-2} (dotted lines), and those that contain at least one star particle (dashed lines). Each curve is coloured by redshift, with lighter colours indicating higher redshifts and darker colours indicating lower redshifts. Note that the range over which we show the field occupation fraction (right) is smaller than for subhaloes in clusters (left). We can see that a small number of subhaloes on the upper end of our probed mass range would be considered observationally dark.

brightness cut (as observed at $z = 0$) of $\langle \mu_V \rangle = 29$ mag arcsec^{-2} to mimic an observational cut.

To illustrate the impact of these cuts, we show in Fig. 3 the occupation fraction ($f_{\rm occ}$) of dark matter subhaloes (left) and haloes (right) as a function of total dark matter mass. We define $f_{\rm occ}$ to be the fraction of (sub)haloes at fixed dark matter mass that host a galaxy. We calculate $f_{\rm occ}$ considering three different cuts on baryonic properties: those with at least 100 star particles or $M_* \geq 8 \times 10^6$ M$_\odot$ (solid lines coloured by redshift), those satisfying the surface brightness requirement (dotted lines colored by redshift), and those that host at least one star particle or gas cell (unresolved baryonic component, dashed lines coloured by redshift).

At $z = 0$ (dark, purple curves), the surface brightness cut implies a very slightly lower occupation fraction for subhaloes with $M_{\rm DM} \lesssim 10^{9.5}$ M$_\odot$. In the field, we find that the surface brightness cuts give an occupation fraction that is much less different from what is found in clusters using particle counts, suggesting that these galaxies should be more luminous or, at least, more compact. Additionally, the closeness between the occupation fraction inferred from particle counts and surface brightness cuts at $z = 0$ is expected in both the field and in clusters, as the surface brightness cut is on par with relatively deep imaging from *Hubble* (see e.g. the Frontier Field; D. Coe et al. 2015; J. M. Lotz et al. 2017).

We do see more of a deviation in the occupation fractions measured from particle counts and surface brightness as redshift increases. This is additionally to be expected, as it becomes more observationally challenging to observe low surface brightness galaxies at higher z. This being said, the surface brightness limits presented here are affected by the too large galaxy sizes predicted by the TNG model at low masses (see A. Pillepich et al. 2018, for a more detailed discussion). The occupation fraction, as measured by surface brightness limits within the simulation, should thus be taken as a conservative upper limit on what is considered observationally resolved.

Investigating $f_{\rm occ}$, including (sub)haloes that possess an unresolved baryonic component (dashed lines in Fig. 3), we see much lower mass objects hosting a potentially luminous component. This is expected and serves simply to show the impact of moving the 'luminous' or resolved threshold in this study. It does, however, show the additional interpretation that many more low-mass galaxies may exist than what our surface brightness limit can probe. In some respects, we could regard this as a manifestation of something like a missing satellites problem, which recent work shows is no longer in tension with ΛCDM (e.g. L. V. Sales et al. 2022, and references therein).

Keeping these limitations in mind, and combining these results with those presented in Fig 2, we find a conservative upper limit of the most massive completely dark subhalo of $M_{\rm DM} \sim 10^{9.5}$ M$_\odot$ in the considered galaxy groups and clusters. These more massive dark objects are exceedingly rare, and tend to only exist at relatively low redshift ($z \lesssim 0.2$). Within the observationally dark limit ($\langle \mu_V \rangle_{\rm h} \gtrsim 29$ mag arcsec^{-2}) in the same environments, we place a similarly conservative upper limit of $M_{\rm DM} \sim 2 \times 10^{10}$ M$_\odot$, which are predominantly present at $z \gtrsim 1$. Extending to the entire TNG50 volume, we find that massive ($M_{\rm DM} \gtrsim 10^{10}$ M$_\odot$), observationally dark objects are more present at all z. We find the most massive entirely dark field object appears at $z = 0$, and has a mass of $M_{\rm DM} \sim 10^{9.75}$ M$_\odot$.

These results may be volume limited. Investigating dark field haloes in the TNG100 simulation (D. Nelson et al. 2018; A. Pillepich et al. 2018, which features the same galaxy formation model as TNG50, but with ∼16× lower resolution), we find the most massive entirely dark object of $M_{\rm DM} = 3.5 \times 10^{10}$ M$_\odot$. Some

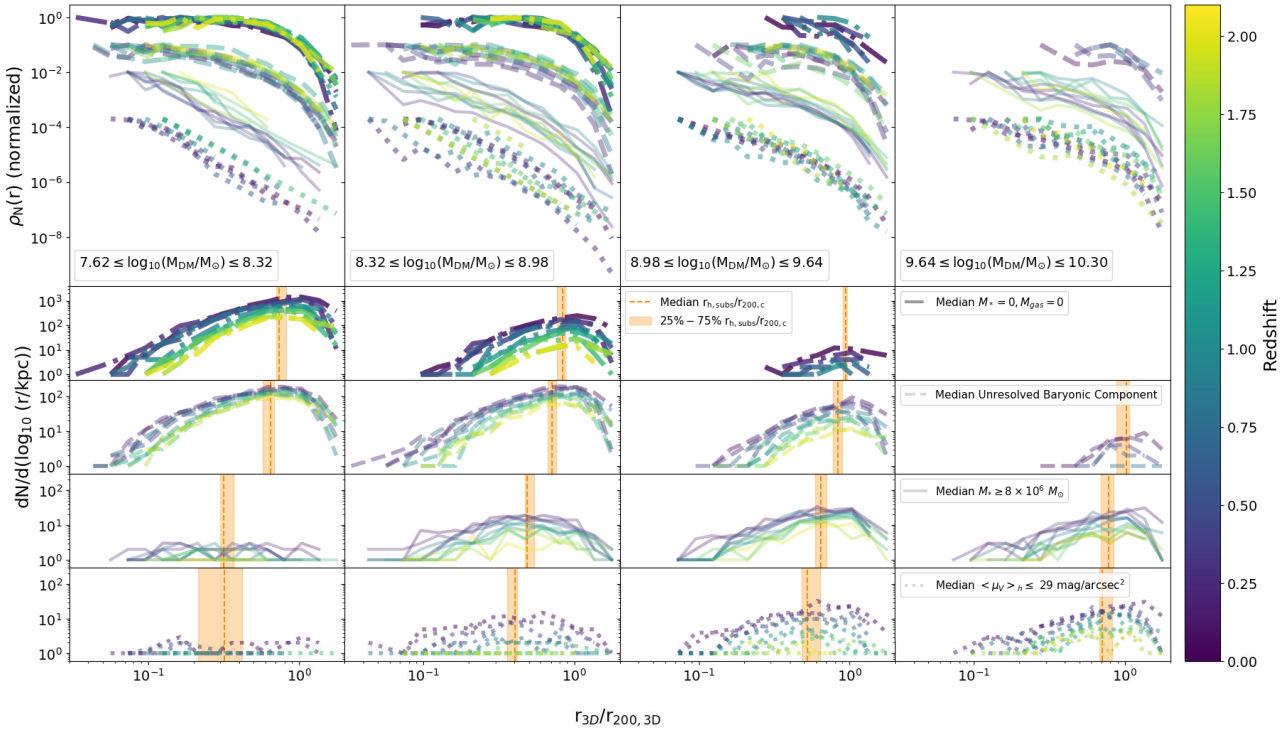

Figure 4. Top panels: The median number density profiles of subhaloes as a function of $r/r_{200,c}$ in our targeted galaxy groups and clusters over time for subhaloes in the mass range $7.62 \leq \log_{10}(M_{DM}) \leq 8.32$ (leftmost panel), $8.32 \leq \log_{10}(M_{DM}) \leq 8.98$ (middle-left panel), $8.98 \leq \log_{10}(M_{DM}) \leq 9.64$ (middle-right panel), and $9.64 \leq \log_{10}(M_{DM}) \leq 10.30$ (rightmost panel). Lower panels: Number of subhaloes per $\log_{10}(r/\mathrm{kpc})$, $\mathrm{d}N/\mathrm{d}\log_{10}(r)$ as a function of $r/r_{200,c}$ for the same mass bins. Each lower panel shows a different component of subhaloes: $M* = 0$, $M_{gas} = 0$ (opaque dot–dashed lines coloured by redshift), those with an unresolved baryonic component (translucent dashed lines), those with $M_* \geq 8 \times 10^6\ \mathrm{M}_\odot$ (transparent lines), and those with $\langle \mu_V \rangle_h \leq 29\ \mathrm{mag\,arcsec}^{-2}$ (translucent dotted lines). Each line in each panel represents the median value of the number (density) between the three target clusters at each radial bin at each redshift. For comparison, we show the median half-number radii and their 25–75 percentile spreads in the verticle orange dashed line and corresponding shaded region, respectively. We can see that while they have a greater half-number radius, dark and observationally dark subhaloes of mass $\log_{10}(M_{DM}/\mathrm{M}_\odot) \leq 8.98$ are most likely, by number, to reside in the strong lensing region of our target groups and clusters at all redshifts.

resolution effects are likely to play a role in this difference as well, so higher resolution studies in larger volumes are necessary to disentangle these effects.

Finally, at any redshift, we expect there to be many more subhaloes that host a low-mass luminous component than what is observed. With better telescopes and deeper surveys, we may yet find that the detection of subhaloes thought to be dark actually contains low-luminosity galaxies. For the upcoming *Habitable Worlds Observatory*, for example, using a set-up involving a 6.5-m mirror, it would be possible to observe even lower surface brightnesses than what is presented in this study. For example, for an object of surface brightnesses of 30 mag arcsec^{-2} could be observed in a ∼1 h exposure with a signal-to-noise ratio of ∼10 in the *V* band.[1]

3.3 Distribution of dark subhaloes in galaxy clusters

We characterize the 3D distribution of subhaloes belonging to our target clusters and their progenitors in Fig. 4. The top panels show the median normalized number density of our target systems' subhaloes as a function of radius at each considered redshift. From left to right, we show this for equally spaced bins of increasing mass, with the leftmost panel showing subhaloes with $7.62 \leq \log_{10}(M_{DM}/\mathrm{M}_\odot) \leq 8.32$, the middle-left panel showing $8.32 \leq \log_{10}(M_{DM}/\mathrm{M}_\odot) \leq 8.98$, the middle-right panel showing $8.98 \leq \log_{10}(M_{DM}/\mathrm{M}_\odot) \leq 9.64$, and the rightmost panel showing $9.64 \leq \log_{10}(M_{DM}/\mathrm{M}_\odot) \leq 10.30$. As in Section 3.2, we investigate three different sets of objects: galaxies resolved by at least 100 star particles (transparent solid lines), those that exceed an average surface brightness within the stellar half-mass radius of 29 mag arcsec^{-2} (transparent dotted lines), and those that possess an unresolved baryonic component (transparent dashed lines). Additionally considered here are subhaloes that are entirely dark ($M_* = 0$, $M_{gas} = 0$, dash–dotted lines). All sets of number density profiles are arbitrarily normalized for ease of interpretation.

Of note in Fig. 4 is that we see some consistency in the slope and shape of each set of luminous or dark subhaloes as a function of redshift. This is expected given the self-similar nature of ΛCDM. Indeed, as found in previous works investigating the distribution of subhaloes in galaxy clusters (e.g. H.-Y. Wu et al. 2013; J. Han et al. 2016), only the normalization of the mass profiles changes between mass bins. While there is some variance in the shape due to the small number statistics in the lowest mass bin, this is insufficient on its own to explain the discrepancy in slope seen in higher mass bins. See Sections 3.4 and 3.5 for additional discussion.

[1] https://hwo.stsci.edu/camera_etc

The bottom four rows of Fig. 4 show the number of subhaloes in given bins of $\log_{10}(r)$ as a function of $r/r_{200,c}$. No normalization has been applied to these curves. Within the inner regions of our selected systems over time, we can see that the subhaloes with $7.62 \leq \log_{10}(M_{DM}/M_\odot) \leq 8.98$ are particularly prevalent. The vast majority of these objects are observationally dark in some way, in that they either possess some unresolved baryonic component or no baryons at all. In the lowest mass bins, very few resolved ($M_* \geq 8 \times 10^6\,M_\odot$) or luminous ($\langle\mu_V\rangle_h \leq 29\,\mathrm{mag\,arcsec^{-2}}$) subhaloes are present, but they tend to distribute at all radii in the clusters. As discussed in Sections 3.1 and 3.2, entirely dark objects with masses $M_{DM} \gtrsim 10^{9.5}\,M_\odot$ are exceptionally rare in clusters (and in the field). While there are a handful of dark subhaloes around this dark matter mass in the most massive clusters in the simulation, the median case is that there are no massive dark subhaloes at any radius within the cluster at any redshift. We do emphasize that only one relatively massive cluster exists in TNG50, so as a limiting case, the presence of massive dark subhaloes in cluster environments can be more conservatively denoted as exceptionally rare in the TNG model.

More quantitatively, we investigate the half-number radius of subhaloes, which we define as the radius that contains half the number of subhaloes in a mass bin within a given group or cluster (denoted by the vertical orange dashed line and corresponding shaded region). While we do find that low-mass (observationally) dark subhaloes tend to be more numerous in the centres of groups and clusters, the half-number radius of these subhaloes tends to be 0.8–0.9 $r_{200,c}$ for dark subhaloes and 0.5–0.8 $r_{200,c}$ for observationally dark objects that host an unresolved baryonic component. For subhaloes with resolved and luminous baryonic components, we find much closer half-number radii, between ∼0.2 and 0.5 $r_{200,c}$ for the two lowest mass bins, and ∼0.5 and 0.8 $r_{200,c}$ for higher mass objects. This mass segregation is expected and can be explained through the mass-dependent time-scale of disruption (e.g. through dynamical friction; see D. Nagai & A. V. Kravtsov 2005; J. Binney & S. Tremaine 2008; F. C. den Bosch et al. 2016; J. Han et al. 2016; T. M. O'Shea et al. 2025). Additionally, the most massive dark subhaloes found within the groups and clusters themselves are very close in mass (within a factor of 2–3) to the most massive dark haloes in the field. Thus, they tend to be the result of recent infall.

3.4 The effect of small number statistics

A more stark disagreement with the predictions from the simulations presented in e.g. D. Nagai & A. V. Kravtsov (2005) and J. Han et al. (2016) is the shape/slope between the two luminous cuts, the observationally dark sample, and the truly dark subhaloes, particularly in the lower mass bins (those in the range $7.62 \leq \log_{10}(M_{DM}/M_\odot) \leq 8.98$). The origin of this discrepancy in the shape of this profile is not entirely trivial. There is, for such low-mass objects, some impact of our choice in what we consider resolved. We can see in Fig. 4 that there are very few luminous objects that are present at any radius within the selected clusters.

We take this as the first test in understanding the discrepant radial distributions in the lowest mass bin. For subhaloes with dark matter masses $7.62 \leq \log_{10}(M_{DM}/M_\odot) \leq 8.32$ that belong to Group 0 at $z = 0$, we subsample a fraction equal to the average occupation fraction within that mass bin 5 per cent to be our new 'luminous' sample. We show the resulting radial number density, $\rho_N(r)$, of this subsampled population in the teal dot–dashed line in the top-left panel of Fig. 5. The nearly power-law relation that is seen in the actual radial distribution of luminous subhaloes is not present in this test. Rather, we find a distribution that agrees well with the distribution of observationally dark subhaloes within the cluster. In the bottom-left panel of Fig. 5, we show the location of the selected subhaloes in the stellar mass–halo mass relation as teal squares. It is perhaps unsurprising that the random selection does not return the same set of (or even a substantial overlap in) subhaloes that actually host a resolved stellar component. It is therefore not exclusively small number statistics that give us the steeper radial distribution of luminous subhaloes in this bin.

3.5 The effect of resolution and mass cuts

While we cannot increase the resolution of the TNG50 simulation, we can turn to a larger volume of the same suite to test the impact of resolution on our results. For this, we invoke the TNG100 simulation (F. Marinacci et al. 2018; J. P. Naiman et al. 2018; D. Nelson et al. 2018; A. Pillepich et al. 2018; V. Springel et al. 2018), which features a $(110.7\ \mathrm{Mpc})^3$ box with a baryonic resolution element having $m_{baryon} = 1.4 \times 10^6\,M_\odot$ and dark matter particle mass of $m_{DM} = 7.5 \times 10^6\,M_\odot$. Within the simulation, we investigate a galaxy cluster of similar mass to Group 0 within TNG50 with $M_{200,c} = 1.73 \times 10^{14}\,M_\odot$. Keeping the same assumption that a minimum of 100 star and/or dark matter particles is considered resolved, we consider subhaloes with a stellar mass of $M_* \geq 1.4 \times 10^8\,M_\odot$ to be luminous.

The rightmost panel of Fig. 5 shows the resulting radial number density distributions in the lowest dark matter mass bin that we can consider with TNG100 ($8.98 \leq \log_{10}(M_{DM}/M_\odot) \leq 9.64$). We can see a very similar behaviour to the lowest mass bin of TNG50, with the luminous subhaloes (light orange solid line) and those with an unresolved baryonic component (pink dashed line) following a steeper distribution than the entirely dark (purple dotted line) subhaloes. Taking the same cuts stellar and dark matter mass cuts in TNG50, however, reveals the same behaviour despite the subhaloes being resolved in this case (see middle panel of Fig. 5). This begs the question: Is this behaviour entirely the result of resolution? Or are we introducing an additional bias in our mass cuts?

It has been noted in the literature that constructing radial distribution by selecting subhaloes based on total mass rather than, for example, infall mass (e.g. $M_{200,c}$) or, by proxy, stellar mass can indeed result in both biases and non-NFW (Navarro–Frenk–White) shapes for radial distributions (e.g. J. Diemand, B. Moore & J. Stadel 2004; L. Gao et al. 2004; D. Nagai & A. V. Kravtsov 2005; J. M. Budzynski et al. 2012; J. Han et al. 2016; B. McDonough & T. G. Brainerd 2022). However, as many of the aforementioned studies note, infall parameters cannot be directly observed. Given that cuts in brightness are inevitable in observational studies, it is important to understand whether or not there is a physical bias in the types of objects that we might be inadvertently selecting for in studies of low-mass galaxies or dark subhaloes in clusters.

Returning to the luminous galaxies in the leftmost panels of Fig. 5, we find that this mass cut biases us to tracing only the subhaloes that have particularly high fractions of stellar mass to dark matter mass ($M_{*,z=0}/M_{DM,z=0} = 0.24$), meaning that these objects tend to be quite tidally stripped of both dark matter ($M_{DM,z=0}/M_{DM,infall} = 0.007$) and stars ($M_{*,z=0}/M_{*,infall} = 0.21$), and have relatively early infall time ($t_{infall} = 2.46$ Gyr) in the median case. For comparison, if we consider the median of all subhaloes with an unresolved baryonic component in this lowest mass bin, we would find much lower fractions of stellar mass to

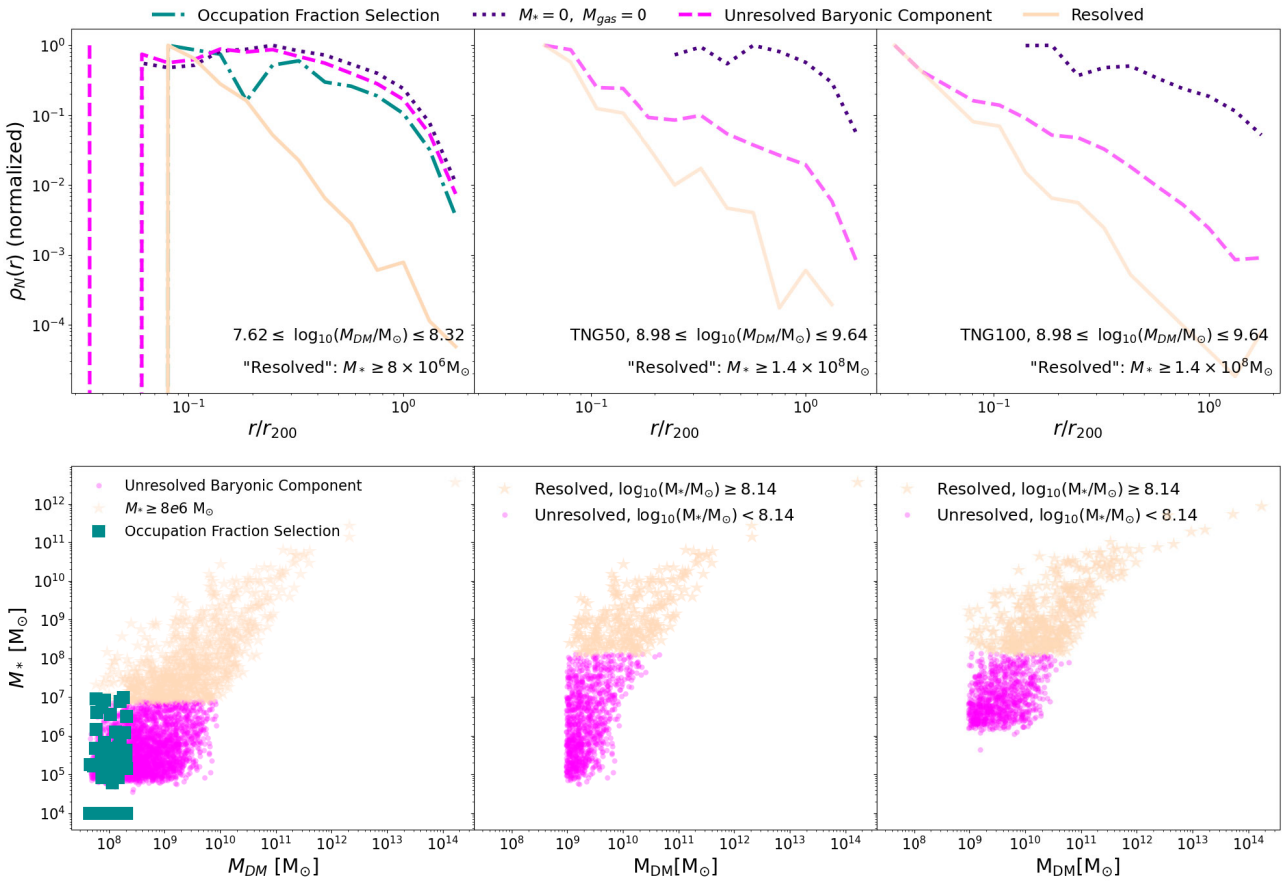

Figure 5. Top: Radial number density profiles that have been normalized to their maximum value. In the leftmost panel of this row, we show the radial number density for the lowest mass bin that we consider in TNG50 ($7.62 \leq \log_{10}(M_{DM}/M_\odot) \leq 8.32$) using only dark objects (purple dotted line), subhaloes with an unresolved baryonic component (pink dashed line), those with a resolved baryonic component (solid light orange line), and using the occupation fraction selection from Section 3.2. We can see that the small number statistics in this case are insufficient to recreate the steepness of the slope of subhaloes with a resolved stellar component. For the middle and rightmost bins, we investigate the lowest mass bin that TNG50 (middle) and TNG100 (right) have in common ($8.98 \leq \log_{10}(M_{DM}/M_\odot) \leq 9.64$). We can see similar behaviour adopting the same mass cuts in both simulations, meaning that resolution is not the only factor in determining the steep slope of the subhaloes with a resolved stellar component. Bottom: Stellar mass–halo mass relation for the lowest mass bin in TNG50 (left), for the more stringent mass cuts in TNG50 (middle) based on the mass cuts in TNG100 (right). The fact that there is a stellar mass cut that interrupts the stellar mass–halo mass relation in each of these bins introduces a bias towards sampling only the highest values of stellar mass from the relation.

dark matter mass ($M_{*,z=0}/M_{DM,z=0} = 0.01$), much higher retained dark matter content ($M_{DM,z=0}/M_{DM,infall} = 0.42$), less stellar stripping by about a factor of 3 ($M_{*,z=0}/M_{*,infall} = 0.64$), and much later infall times ($t_{infall} = 8.08$ Gyr). As we move to higher dark matter mass bins, we find that the fraction of stellar mass to dark matter mass for luminous objects until it levels out around 0.02; the fraction of dark matter and stellar mass retained after infall increases; and the median infall time increases. We therefore conclude that in a dark matter mass bin that contains an imposed stellar mass cut, the resulting luminous galaxies will be among the oldest and most tidally stripped within the cluster.

4 DISCUSSION: IMPLICATIONS FOR DARK SUBHALO SEARCHES

The previous sections have illustrated that there are several complicating factors in understanding truly dark subhaloes in galaxy groups and clusters. Within the target systems we trace over time in TNG50, and at all redshifts, we find very few massive dark (sub)haloes. This is not unexpected: galaxy formation theory asserts that all haloes with a virial temperature, $T_{vir} \sim 2000$ K, or, equivalently, a mass $M_{200,c} \gtrsim 10^{9.7}\ M_\odot$, can cool gas and form stars (see e.g. M. J. Rees 1986; G. Efstathiou 1992; T. Quinn et al. 1996; A. A. Thoul & D. H. Weinberg 1996; R. Barkana & A. Loeb 1999; T. Sawala et al. 2016; A. Benitez-Llambay & C. Frenk 2020). This is reflected quite clearly in the occupation fraction of resolved galaxies in field haloes (see Fig. 3). These objects are expected to lose mass after they infall into their present-day group or cluster (e.g. D. Nagai & A. V. Kravtsov 2005; J. Binney & S. Tremaine 2008; J. Han et al. 2016; T. M. O'Shea et al. 2025), so massive dark objects are expected to be rarer in clusters.

Our conclusions have, thus far, been investigated in 3D space rather than in projection. The effects of (dark) objects on a strongly lensed image are cumulative; objects in the field along the line of sight need to be taken into account. As an albeit simplistic test of the impact of line-of-sight haloes on our previous results, we have taken 'observations' of our target groups and clusters as though they are centred in a cylinder the length of the simulation volume ($L = 51.7$ Mpc) with a radius $2R_{200,c}$ from their centres along a grid of 36 different sightlines. We show

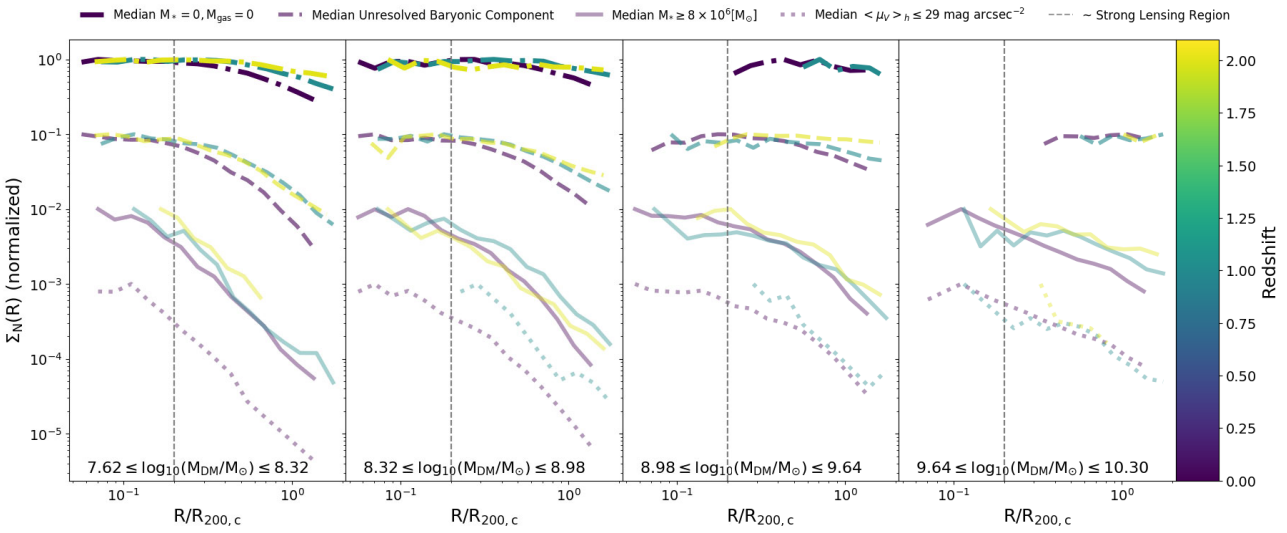

Figure 6. Median projected number density profiles of subhaloes along 36 different sightlines centred on our target clusters in TNG50 over time. For clarity, we show this for only $z = 0$, 1, and 2. The profiles have been arbitrarily normalized to highlight their differences in shape. Each panel represents a different mass bin as in Fig. 4. We can see, as expected, qualitatively flatter shapes, due to the effects of projection. Given the integrated nature of gravitational lensing, low-mass subhaloes both from the cluster itself and from the field are more likely to be found around the strong lensing region than suggested by the 3D profiles.

the resulting inferred median projected radial profiles of each component in Fig. 6. We can see that the profiles, particularly in the lowest mass bins, tend towards flatter shapes than in their 3D, cluster-only counterparts. For reference, we show an approximate strong lensing region as the dotted black line in each panel of the plot, which corresponds to the same mass bins as in Fig. 4.

Fig. 7 shows the resulting median projected half-number radius of (sub)haloes, their respective mass bins, and populations – those that are dark ($M_* = 0$, $M_{\rm gas} = 0$), those that have an unresolved baryonic component, those that are resolved with $M_* \geq 8 \times 10^6\,{\rm M}_\odot$, and those that are luminous ($\langle\mu_V\rangle_{\rm h} \leq 29\,{\rm mag\,arcsec^{-2}}$) – as a function of the host's halo mass, $M_{200,{\rm c}}$. As in Fig. 4, we see a similar, though expected, trend that lower mass subhaloes (circles and squares coloured by redshift of the host group) tend to reside closer to the centres of their hosts than higher mass subhaloes (stars and plus signs). We do, however, though somewhat unsurprisingly, find that the half-number radii, when deprojected (assuming $R_{\rm proj} = 0.75 r_{\rm 3D}$ as in e.g. L. Hernquist 1990; J. Wolf et al. 2010; R. S. Somerville et al. 2018) are larger for the set of entirely dark objects (top panel of Fig. 7) and those with an unresolved baryonic component (following panel of Fig. 7) than would be expected of the distribution of subhaloes when considering groups and clusters in isolation. Conversely, we see smaller half-number radii for objects that host a resolved stellar component ($M_* \geq 8 \times 10^6\,{\rm M}_\odot$, next to last panel of Fig. 7), and those that are luminous ($\langle\mu_V\rangle_{\rm h} \leq 29\,{\rm mag\,arcsec^{-2}}$, bottom panel of Fig. 7).

Both of these effects can be traced to the differing occupation fraction of subhaloes in groups and clusters and field haloes. As can be seen in Fig. 3, there is a higher mass turnover in the occupation fraction for all considered sets of galaxies. Thus, for (observationally) dark objects, the increase of line-of-sight objects causes a flattening out of the radial distribution. This acts to pull the half-number radii further out. For (sub)haloes that satisfy the star particle number cut and surface brightness cut, we find radial profiles that are *steeper* than expected considering only the target cluster in isolation. This is particularly prevalent in the lowest mass bin (circles in Fig. 7), where the radial profiles are already quite steep as a result of our chosen stellar mass and surface brightness cuts.

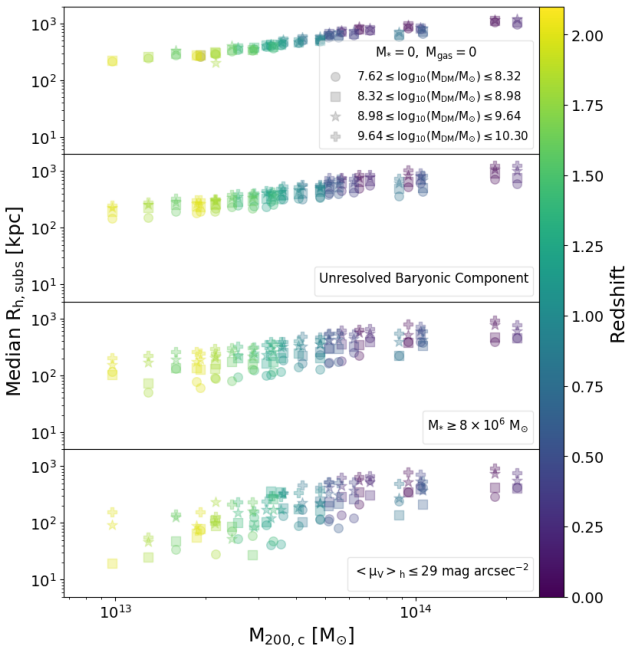

Figure 7. Median half-number radius for dark (top), unresolved (panel 2), resolved (panel 3), and luminous (bottom) of 36 projected directions centred on each cluster progenitor. We can see that even in projected space, we are more likely to find lower mass subhaloes (circles and squares) closer to the centres of their hosts than higher mass subhaloes (stars and plus signs). Interestingly, the half-number radius of dark things is roughly half the radius of the projected area, illustrating that these objects are roughly uniformly distributed in a projected configuration.

The detection of a truly dark subhalo could provide a test of both ΛCDM and our current galaxy formation framework. In order for such objects to be (indirectly) observationally detected at galaxy group or cluster scales by invoking strong gravitational lensing, a dark subhalo would need to exist very near the strong lensing region ($R \sim 10$–250 kpc from the centre of a cluster). We show a radius of 250 kpc for the most massive cluster in TNG50 at $z = 0$ by the vertical black dotted line in Fig. 6. Investigating the number of subhaloes at this radius at $z \sim 0$, we find a total of ∼100 entirely dark subhaloes that mostly reside in the mass range $7.62 \leq \log_{10}(M_{\rm DM}/{\rm M}_\odot) \leq 8.32$, with a similar total number of subhaloes with an unresolved baryonic component, most of which exist in the range $7.62 \leq \log_{10}(M_{\rm DM}/{\rm M}_\odot) \leq 8.98$. There are ∼20 total subhaloes that host a resolved or luminous galaxy. Thus, as expected from a ΛCDM framework, low-mass objects, in particular those that are found to be (observationally) dark in this study, are most likely to be found in this region.

5 SUMMARY

In this study, we have utilized the three most massive galaxy groups and clusters, as well as their progenitors from $0 \leq z \lesssim 2$, in the TNG50 simulation to investigate their populations of low-mass subhaloes ($4.54 \times 10^7 \leq M_{\rm DM}/{\rm M}_\odot \leq 2 \times 10^{10}$). We find that:

(i) Massive dark (sub)haloes ($M_{\rm DM} \gtrsim 10^{9.7}\,{\rm M}_\odot$) are rare, which is expected from galaxy formation theory, which places a mass limit of $M_{200,{\rm c}} \lesssim 10^{10}\,{\rm M}_\odot$ on objects that will always form stars.

(ii) While it is unsurprising that faint objects are not easily detected at any redshifts, they are particularly relevant to consider in subhalo studies. With an inferred occupation fraction of $f_{\rm occ}(< 1)$ still by $M_{\rm DM} = 10^{10}\,{\rm M}_\odot$ at $z \sim 2$, it is entirely feasible that a faint dwarf galaxy may reside in detected massive subhaloes. This discrepancy alleviates itself at lower redshift, simply by the nature of an increased ease of observation of low-mass objects.

(iii) Both dark and observationally dark subhaloes reside at all radii in galaxy groups and clusters. It is low-mass, $M_{\rm DM} \lesssim 10^{8.32}\,{\rm M}_\odot$, subhaloes that are most likely, by number, to be dark and reside in the strong lensing regions of galaxy groups and clusters.

(iv) Taking into account the effects of line-of-sight haloes and subhaloes, we find flatter distributions of dark and observationally dark subhaloes within $2R_{200,{\rm c}}$ of their host groups and clusters at all redshifts. However, we similarly find it rare for dark subhaloes with masses $M_{\rm DM} \gtrsim 10^9\,{\rm M}_\odot$ to exist in the strong lensing regions of groups and clusters.

It is important to note that the above results are *conservative* estimates for the expected properties of dark and observationally (sub)haloes. First, we have sacrificed working with larger volumes with higher mass galaxy clusters in favour of increased resolution in this study. There may be volume effects that are outside of the scope of this study to investigate. Second, low-mass galaxies in the TNG galaxy formation model tend to be puffier than expected, meaning that the predicted surface brightnesses are likely lower than expected as well. We thus expect an overprediction of observationally dark objects (see A. Pillepich et al. 2018). The resolution limit may imply that the absence of stars and gas in entirely dark objects is rather indicative of simply possessing a stellar or gaseous component that is below the resolution limit of the simulation. Finally, we thus emphasize that our results should be taken as upper limits for both mass and the number of dark and observationally dark objects.

Observational tests are, of course, necessary to confirm the predictions set forth in this work. Several studies have made potential detections of subhaloes with masses greater than $10^9\,{\rm M}_\odot$ (e.g. S. Vegetti et al. 2010, 2012; S. C. Lange et al. 2025). Assuming the conditions explored in this study, it is unlikely that they should be dark. Therefore, to probe the low-mass objects that should be numerous in the strong lensing regions of galaxy clusters, extremely high-resolution imaging and extremely deep observations are necessary, such as those anticipated for the *Habitable Worlds Observatory*.

ACKNOWLEDGEMENTS

We thank the referee for a useful report that improved the previous iteration of this paper. JED, MJ, and DJL are supported by the United Kingdom Research and Innovation (UKRI) Future Leaders Fellowship 'Using Cosmic Beasts to Uncover the Nature of Dark Matter' (grant no MR/X006069/1). DJL was also supported by Science and Technology Facilities Council (STFC) grants ST/T000244/1 and ST/W002612/1. AF acknowledges support of a UKRI Future Leaders Fellowship (grant no. MR/T042362/1) and a Wallenberg Academy Fellowship. This work used the DiRAC@Durham facility managed by the Institute for Computational Cosmology on behalf of the STFC DiRAC HPC Facility (www.dirac.ac.uk). The equipment was funded by Business, Energy and Industrial Strategy (BEIS) capital funding via STFC capital grants ST/K00042X/1, ST/P002293/1, ST/R002371/1, and ST/S002502/1, Durham University, and STFC operations grant ST/R000832/1. DiRAC is part of the National e-Infrastructure.

This study has made use of the following open-source software that we would like to acknowledge here: H5PY (A. Collette et al. 2022), MATPLOTLIB (J. D. Hunter 2007), NUMPY (C. R. Harris et al. 2020), and SCIPY (P. Virtanen et al. 2020; R. Gommers et al. 2022).

DATA AVAILABILITY

The work presented in this paper utilizes halo catalogues and merger trees from the IllustrisTNG project (D. Nelson et al. 2019a). The data are publicly available at https://www.tng-project.org/.

REFERENCES

Ahvazi N., Benson A., Sales L. V., Nadler E. O., Weerasooriya S., Du X., Bovill M. S., 2024, MNRAS, 529, 3387
Atek H. et al., 2025, preprint (arXiv:2511.07542)
Barkana R., Loeb A., 1999, ApJ, 523, 54
Benitez-Llambay A., Frenk C., 2020, MNRAS, 498, 4887
Benson A. J., Lacey C. G., Baugh C. M., Cole S., Frenk C. S., 2002, MNRAS, 333, 156
Binney J., Tremaine S., 2008, Galactic Dynamics, 2nd edn. Princeton Univ. Press, Princeton, NJ
Bleem L. E. et al., 2015, ApJS, 216, 27
Bonaca A., Hogg D. W., Price-Whelan A. M., Conroy C., 2019, ApJ, 880, 38
Budzynski J. M., Koposov S. E., McCarthy I. G., McGee S. L., Belokurov V., 2012, MNRAS, 423, 104
Bullock J. S., Boylan-Kolchin M., 2017, ARA&A, 55, 343
Bullock J. S., Kravtsov A. V., Weinberg D. H., 2000, ApJ, 539, 517
Carlberg R. G., 2012, ApJ, 748, 20

Cerny C. et al., 2025, preprint (arXiv:2503.17498)
Coe D., Bradley L., Zitrin A., 2015, ApJ, 800, 84
Coe D. et al., 2019, ApJ, 884, 85
Collette A. et al., 2022, h5py/h5py: 3.7.0. Zenodo. https://doi.org/10.5281/zenodo.6575970
Crain R. A. et al., 2015, MNRAS, 450, 1937
Davis M., Efstathiou G., Frenk C. S., White S. D. M., 1985, ApJ, 292, 371
Dehnen W., Odenkirchen M., Grebel E. K., Rix H.-W., 2004, AJ, 127, 2753
Diego J. M. et al., 2018, ApJ, 857, 25
Diego J. M., Pascale M., Kavanagh B. J., Kelly P., Dai L., Frye B., Broadhurst T., 2022, A&A, 665, A134
Diego J. M. et al., 2023, A&A, 679, A31
Diemand J., Moore B., Stadel J., 2004, MNRAS, 353, 624
Dolag K., Borgani S., Murante G., Springel V., 2009, MNRAS, 399, 497
Drinkwater M. J., Gregg M. D., Colless M., 2001, ApJ, 548, L139
Efstathiou G., 1992, MNRAS, 256, 43P
Euclid Collaboration, 2025, preprint (arXiv:2503.15330)
Forouhar Moreno V. J., Benítez-Llambay A., Cole S., Frenk C., 2022, MNRAS, 517, 5627
Forouhar Moreno V. J., Helly J., McGibbon R., Schaye J., Schaller M., Han J., Kugel R., Bahé Y. M., 2025, MNRAS, 543, 1339
Fox C., Mahler G., Sharon K., Remolina González J. D., 2022, ApJ, 928, 87
Gaia Collaboration, 2016, A&A, 595, A1
Gámez-Marín M., Santos-Santos I., Domínguez-Tenreiro R., Pedrosa S. E., Tissera P. B., Gómez-Flechoso M. Á., Artal H., 2024, ApJ, 965, 154
Gao L., White S. D. M., Jenkins A., Stoehr F., Springel V., 2004, MNRAS, 355, 819
Genel S. et al., 2014, MNRAS, 445, 175
Ghigna S., Moore B., Governato F., Lake G., Quinn T., Stadel J., 1998, MNRAS, 300, 146
Gnedin O. Y., 2003, ApJ, 589, 752
Gommers R. et al., 2022, scipy/scipy: SciPy 1.9.1. Zenodo
Gonzalez E. J., Foëx G., Nilo Castellón J. L., Domínguez Romero M. J., Alonso M. V., García Lambas D., Moreschi O., Gallo E., 2015, MNRAS, 452, 2225
Han J., Cole S., Frenk C. S., Jing Y., 2016, MNRAS, 457, 1208
Harris C. R. et al., 2020, Nature, 585, 357
Hernquist L., 1990, ApJ, 356, 359
Hezaveh Y. D. et al., 2016, ApJ, 823, 37
Hunter J. D., 2007, Comput. Sci. Eng., 9, 90
Jahn E. D., Sales L. V., Wetzel A., Boylan-Kolchin M., Chan T. K., El-Badry K., Lazar A., Bullock J. S., 2019, MNRAS, 489, 5348
Jauzac M. et al., 2014, MNRAS, 443, 1549
Kim S. Y. et al., 2024, preprint (arXiv:2408.15214)
Lagattuta D. J. et al., 2023, MNRAS, 522, 1091
Lange S. C. et al., 2025, MNRAS, 539, 704
Lee G., Hwang H. S., Lee J., Shin J., Song H., 2024, ApJ, 962, 129
Lotz J. M. et al., 2017, ApJ, 837, 97
McDonough B., Brainerd T. G., 2022, ApJ, 933, 161
Mahler G. et al., 2023, ApJ, 945, 49
Marinacci F. et al., 2018, MNRAS, 480, 5113
Mei S. et al., 2007, ApJ, 655, 144
Monzon J. S., van den Bosch F. C., Mitra K., 2024, ApJ, 976, 197
Moore B., Katz N., Lake G., Dressler A., Oemler A., 1996, Nature, 379, 613
Munshi F., Brooks A. M., Applebaum E., Christensen C. R., Quinn T., Sligh S., 2021, ApJ, 923, 35
Nadler E. O., 2025, ApJ, 983, L23
Nadler E. O. et al., 2020, ApJ, 893, 48
Nadler E. O., Gluscevic V., Driskell T., Wechsler R. H., Moustakas L. A., Benson A., Mao Y.-Y., 2024, ApJ, 967, 61
Nagai D., Kravtsov A. V., 2005, ApJ, 618, 557
Naiman J. P. et al., 2018, MNRAS, 477, 1206
Natarajan P., Williams L. L. R., Bradač M., Grillo C., Ghosh A., Sharon K., Wagner J., 2024, Space Sci. Rev., 220, 19
Nelson D. et al., 2018, MNRAS, 475, 624
Nelson D. et al., 2019a, Comput. Astrophys. Cosmol., 6, 2
Nelson D. et al., 2019b, MNRAS, 490, 3234
Niemiec A., Jullo E., Giocoli C., Limousin M., Jauzac M., 2019, MNRAS, 487, 653
Nierenberg A. M., Treu T., Wright S. A., Fassnacht C. D., Auger M. W., 2014, MNRAS, 442, 2434
O'Shea T. M., Borrow J., O'Neil S., Vogelsberger M., 2025, Open J. Astrophys., 8, 17E165
Pakmor R., Springel V., 2013, MNRAS, 432, 176
Pakmor R., Bauer A., Springel V., 2011, MNRAS, 418, 1392
Pillepich A. et al., 2018, MNRAS, 475, 648
Pillepich A. et al., 2019, MNRAS, 490, 3196
Planck Collaboration XIII, 2016, A&A, 594, A13
Postman M. et al., 2012, ApJS, 199, 25
Quinn T., Katz N., Efstathiou G., 1996, MNRAS, 278, L49
Rees M. J., 1986, MNRAS, 218, 25P
Rey M. P. et al., 2025, MNRAS, 541, 1195
Richard J. et al., 2021, A&A, 646, A83
Rodriguez-Gomez V. et al., 2015, MNRAS, 449, 49
Sales L. V., Wetzel A., Fattahi A., 2022, Nat. Astron., 6, 897
Sands I. S. et al., 2024, preprint (arXiv:2404.16247)
Sawala T., Frenk C. S., Crain R. A., Jenkins A., Schaye J., Theuns T., Zavala J., 2013, MNRAS, 431, 1366
Sawala T. et al., 2016, MNRAS, 456, 85
Schaye J. et al., 2015, MNRAS, 446, 521
Schaye J. et al., 2023, MNRAS, 526, 4978
Sharon K. et al., 2020, ApJS, 247, 12
Sheth R. K., Mo H. J., Tormen G., 2001, MNRAS, 323, 1
Shuntov M. et al., 2022, A&A, 664, A61
Shuntov M. et al., 2025, A&A, 695, A20
Simon J. D., 2019, ARA&A, 57, 375
Smith R., Choi H., Lee J., Rhee J., Sanchez-Janssen R., Yi S. K., 2016, ApJ, 833, 109
Somerville R. S. et al., 2018, MNRAS, 473, 2714
Springel V., White S. D. M., Tormen G., Kauffmann G., 2001, MNRAS, 328, 726
Springel V. et al., 2018, MNRAS, 475, 676
Strigari L. E., 2013, Phys. Rep., 531, 1
Thoul A. A., Weinberg D. H., 1996, ApJ, 465, 608
van den Bosch F. C., Jiang F., Campbell D., Behroozi P., 2016, MNRAS, 455, 158
van den Bosch F. C., Ogiya G., Hahn O., Burkert A., 2018, MNRAS, 474, 3043
Vegetti S., Koopmans L. V. E., Bolton A., Treu T., Gavazzi R., 2010, MNRAS, 408, 1969
Vegetti S., Lagattuta D. J., McKean J. P., Auger M. W., Fassnacht C. D., Koopmans L. V. E., 2012, Nature, 481, 341
Vegetti S., Koopmans L. V. E., Auger M. W., Treu T., Bolton A. S., 2014, MNRAS, 442, 2017
Virtanen P. et al., 2020, Nat. Med., 17, 261
Vogelsberger M. et al., 2014, MNRAS, 444, 1518
Wechsler R. H., Tinker J. L., 2018, ARA&A, 56, 435
Weinberger R. et al., 2017, MNRAS, 465, 3291
Weinmann S. M., Lisker T., Guo Q., Meyer H. T., Janz J., 2011, MNRAS, 416, 1197
White S. D. M., Frenk C. S., 1991, ApJ, 379, 52
White S. D. M., Rees M. J., 1978, MNRAS, 183, 341
Wolf J., Martinez G. D., Bullock J. S., Kaplinghat M., Geha M., Muñoz R. R., Simon J. D., Avedo F. F., 2010, MNRAS, 406, 1220
Wu H.-Y., Hahn O., Wechsler R. H., Behroozi P. S., Mao Y.-Y., 2013, ApJ, 767, 23
Yoon J. H., Johnston K. V., Hogg D. W., 2011, ApJ, 731, 58

This paper has been typeset from a TEX/LATEX file prepared by the author.